# On the structure of turbulent gravel bed flow: implications for sediment transport

Seyed Hossein Mohajeri[a,b,*], Maurizio Righetti[c], Geraldene Wharton[b],
Giovanni Paolo Romano[d]

[a] *Department of Civil, Mechanics and Environmental Engineering, University of Trento, Trento, Italy.*
[b] *School of Geography, Queen Mary University of London, London E1 4NS, UK.*
[c] *Faculty of Science and technology, Free University of Bozen, Bozen, Italy.*
[d] *Department of Mechanical and Aeronautical Engineering, University "La Sapienza", Via Eudossiana 18-00184 Roma, Italy.*

---

## Abstract

The main objective of this study was to examine the turbulent flow field over gravel particles as a first step towards understanding sediment transport in a gravel bed river. Specifically, the vertical momentum flux in gravel bed turbulent flow was investigated with particular attention to the near-bed region. Spatial organization of vertical momentum flux was studied with stereoscopic Particle Image Velocimetry (PIV) measurements in a horizontal layer 1mm above the gravel crests. The vertical momentum flux through the water column was described with digital PIV measurements in three vertical planes. The data showed that near the gravel bed, net turbulent momentum flux spatially varies with respect to bed topography. Analysis of the vertical velocity data revealed that near the gravel particle crests, there is a significant net vertical form-induced momentum flux approximately with the same order of magnitude as the net vertical turbulent momentum flux. Above the crests, total net vertical momentum flux is positive. However, below the crests, despite noticeable positive form-induced momentum flux, total net vertical momentum flux is negative. Results of quadrant analysis show that variation of turbulent net vertical momentum

---

[*] Corresponding author

*Email addresses:* `hossein.mohajeri@unitn.it` (Seyed Hossein Mohajeri), `maurizio.righetti@unibz.it` (Maurizio Righetti), `g.wharton@qmul.ac.uk` (Geraldene Wharton), `romano@dma.ing.uniroma1.it` (Giovanni Paolo Romano)

flux through water column is in agreement with prevalence of upward movement of low velocity flow (known as ejection) above gravel crests and downward movement of high velocity flow (known as sweep) below gravel crests. Below gravel crests ($-0.1 < z/H < 0.0$), there is a region where the contribution of second quadrant to Reynolds shear stress is lower than fourth quadrant, while the contribution of second quadrant to vertical momentum flux is higher than fourth quadrant. This can be interpreted that ejection events in this region are strong enough to lift up fine particles but their contribution is not sufficient to move fine particles in the longitudinal direction.

*Keywords:* Gravel Bed, Sediment Transport, Turbulent Flow, Bursting Process, Vertical Velocity.

## 1. Introduction

Transport and deposition of fine sediments above gravel bed rivers is common especially in mountainous areas [1, 2]. Improved knowledge of the distinct characteristics of fine sediments, which affects their erodibility [3] and the flow structures above gravel beds will further our understanding of fine sediment dynamics. This is important because fine sediments deliver benefits such as a nutrient supply to biota living in the fluvial system, but excessive fine sediment loads and the presence of sediment-bound contaminants can cause significant environmental impacts [4, 5]. Deposition of finer material in the matrix of a gravel bed and its filtration to the deeper layer (known as colmation) affects the fluvial system by reducing hydraulic conductivity [6, 7] and can alter the physical, chemical and biological properties of the hyporheic zone and benthic layer [7]. Decolmation, the entrainment of fine particles from the matrix of a gravel bed, also impacts the fluvial system by increasing the surface and subsurface inter-connection [8]. As a consequence, fish spawning and incubation, invertebrate development, oxygen availability, and microbial activity can all be affected by colmation and decolmation [9, 10].

Transport of fine sediment in a free surface flow is triggered by near-bed turbulence [11, 12, 13, 14]. The interaction between particles and bed turbulence influences the diffusion and transport processes of suspended sediment in the outer part of the flow field. Different studies on the structure of turbulent flow have recognized the importance of the near-bed bursting-sweep cycle for particle entrainment and transport [13, 14, 15, 16]. Bursting is a phenomenon common in the turbulent boundary layer and open channels and provides evidence of the presence of turbulent coherent structures that develop in the near-bed region of the flow field. It comprises a quasi-cyclic process of the upward motion of low-velocity fluid parcels (ejection) and downward motion of high-velocity parcels (sweep) [17], which are associated with short-duration large-amplitude wall pressure fluctuations [18, 19]. Many studies demonstrated the role of intense wall pressure fluctuations in sediment transport [20, 21, 22]. Dwivedi et al. [20, 22] show that vertical and horizontal pressure gradients resulting from wall pressure fluctuations are important for sediment entrainment. According to Detert et al. [22], pressure fluctuations can cause sediment entrainment. Although the reasoning of Detert et al. [22] and Dwivedi et al. [20, 22] is slightly different, both agreed that sediments are more probably entrained during sweep events. However, at high flow rate and bed-load discharge Radice et al. [23] found high correlation of bed load transport with ejection events.

Recent developments in research suggest a turbulent burst is the outcome of a succession of ejections due to the passage of a packet of hairpin vortices [24]. The bursting process in the near-wall region interacts with large scale coherent structures in outer layer [24, 25, 26] and is considered to play an important role in the overall dynamics of the boundary layer and sediment transport processes. Ejections are considered to be primarily responsible for particle entrainment and resuspension [11, 16, 27, 28, 29, 30, 31] whereas transport of of fine sediment as bed load is mostly attributed to sweeps impinging on the bed [32, 33].

There is experimental evidence that the main features of bursting phenomena are common on both smooth and rough beds [25, 27, 31]. On the other hand, there are fundamental differences between the two classes of beds. In smooth wall conditions, bursting is related to flow instabilities taking place in the alternating high and low velocity streaks belonging to the viscous sublayer, while for a rough bed, the protrusion of roughness elements disrupts the viscous sublayer and buffer layer and bursting seems to be triggered by the wake-like vortex shedding at roughness crests [34, 35, 36]. Moreover, these features of the bursting phenomena in gravel bed flow are accompanied by the experimental evidence that for this kind of flow the time-averaged velocity field and higher order turbulence moments at the near-bed region (known as *roughness layer* in fluid mechanics studies [37, 38, 39]) vary spatially in accordance with bed topography [40, 41].

To properly consider the near-bed spatial variability of the flow in transport equations, locally time-averaged flow characteristics should also be averaged in space, which leads to the Double-Averaged Navier-Stokes (DANS) equations [42, 43, 44]. In DANS equations viscous drag, form drag, and correlation of spatial fluctuation of time-averaged velocities (known as form-induced stresses) are explicitly expressed [44]. Form-induced stresses in DANS equations contribute momentum flux in addition to Reynolds stresses [45]. Despite the common use of the double averaging method in rough bed flow studies, vertical momentum transport has not been examined in detail by applying the double averaging method. Specifically, the spatial organization of near-bed vertical momentum flux has not been properly described and the importance of form-induced stresses in vertical momentum flux and in comparison to double-averaged vertical Reynolds stress has not been fully addressed.

The aim of the present study is to analyse those characteristics of turbulent flow which are important for the vertical transport. First, the vertical velocity and vertical momentum flux over a gravel bed was studied through application of the extended Wei and Willmarth's [28] method by applying the double averaging method. The extension of Wei and Willmarth [28]'s analysis through the double averaging method improves understanding of the role of near-bed turbulence heterogeneity and form-induced stresses in vertical momentum flux. Secondly, to demonstrate the relationship between spatial variations of vertical momentum flux and the bursting process, quadrant analysis was applied to the experimental data.

The flow field was measured experimentally through the PIV technique [46, 47]. All experimental measurements and analyses were conducted for flows over a fixed gravel bed in the absence of fine sediments. Any addition of fine sediment particles in the flow field could lead to unwanted misunderstanding in the velocity signal measured with PIV. This is because even very small sediment particles may not exactly follow the flow and therefore have different velocities with respect to the water and can give an optical signal for the PIV as tracer particles. This can be particularly true at the near-bed region (see as an example, [30]). Working in clear water allowed the authors to avoid this potential source of error in the water velocity signal and so clearly depict the aspects of the flow fields previously mentioned and establish its implications for sediment transport. The clear water experiments discussed in the paper could be extended in the future by investigating fine sediment-laden flows on immobile gravel, or at least an experimental set-up of cobbles partially covered by fine sediments. In this case the overall effect could be seen as a first approximation, in its simplest form the reduction of the absolute bed roughness of the gravel bed (e.g. reduction of inter-cobbles cavities depths due to partial filling by sand). Moreover, the aim of the present work was not to consider the "*two-phase*" flow which does not consider the effect of particle-particle or fluid-particle interaction. The results of the present study can inform understanding of the basic mechanisms of the entrainment and deposition of fine particles on an immobile gravel bed in relation to the flow structure in the near-bed region. The "*closure*" of the problem of an "*equilirium*" sediment laden flow over a gravel bed is beyond the aim of the paper.

## 2. Theoretical Background

According to the double averaging methodology in steady, uniform, rough bed, open channel flow, the following simplifying assumptions are generally applied: 1) $\partial\langle \ \bar{}\ \rangle/\partial x = 0$; 2) $\partial \ \bar{}\ /\partial t = 0$ 3) $\langle \overline{w} \rangle = 0$, where the overbar denotes a time/ensemble average and the angle brackets denote a spatial average. As a result, the double-averaged momentum transport equation in vertical direction reduces to [39]:

$$-gcos\theta - \frac{1}{\rho}\frac{1}{\Phi}\frac{\Phi\partial\langle\overline{p}\rangle}{\partial z} + \frac{1}{\Phi}\frac{\Phi\partial\langle -\overline{w'^2}\rangle}{\partial z} + \frac{1}{\Phi}\frac{\Phi\partial\langle -\tilde{w}^2\rangle}{\partial z} + \nu\nabla(\Phi\nabla\partial\langle\overline{w}\rangle) = 0 \tag{1}$$

where prime shows turbulent fluctuations in time and tilde shows deviations of the time-averaged velocities from their double-averaged counterparts (i.e. $\tilde{w} = \overline{w} - \langle\overline{w}\rangle$ and $w = \langle\overline{w}\rangle + \tilde{w} + w'$), $\theta$ is the angle between the bed and the horizontal line, $w$ is vertical velocity, $p$ is pressure, $g$ is gravitational acceleration, $\rho$ is fluid density, $\nu$ is viscosity and $\Phi$ is roughness geometry function which is defined as the ratio of the area occupied by fluid to the total area of the averaging domain that includes, below roughness crests, the gravel particles [39]. By neglecting the effect of viscosity ($\nu(\nabla\Phi\nabla\partial\langle\overline{w}\rangle) \approx 0.0$), this equation after integration along water depth leads to:

$$\langle\overline{p}\rangle = \rho\,(H-z)\,cos\theta - \rho\left\langle\overline{w'^2}\right\rangle - \rho\left\langle\tilde{w}^2\right\rangle - \int_z^{z_c}\left[\frac{1}{\Phi}\frac{\partial\Phi}{\partial z}(\rho\left\langle\overline{w'^2}\right\rangle + \rho\left\langle\tilde{w}^2\right\rangle + \langle\overline{p}\rangle\,)\right]dz \tag{2}$$

In Eq. 2, $(H-z)cos\theta$ is static pressure, $\rho\left\langle\overline{w'^2}\right\rangle$ and $\rho\left\langle\tilde{w}^2\right\rangle$ are double-averaged vertical Reynolds stress and vertical form-induced stress, which represent vertical momentum fluxes. The last term in Eq. 2 is the result of vertical variation of the roughness geometry function with upper limit of integration, $z_c$, equal to bed material (in present study gravel) crest. Double-averaged vertical Reynolds stress is turbulent momentum flux and the vertical form-induced stress is the transfer of local momentum caused by spatial disturbances in time-averaged flow [45, 39]. Form-induced stresses are important in the region below the gravel crests (known as the *interfacial sub-layer*, sensu Nikora et al. [39]) and in a region slightly above the gravel crests (known as the *form-induced sub-layer* sensu Nikora et al. [39]). These two sub-layers together are generally called the roughness layer.

Nevertheless, Eq. 2 shows that above the gravel crests, where the integral of the last term in Eq. 2 is zero, double-averaged pressure ($\langle \bar{p} \rangle$ ) is only composed of static pressure ($\rho(H-z)cos\theta$) and a form of *"dynamic pressure"*($\rho \left\langle \overline{w'^2} \right\rangle + \rho \left\langle \tilde{w}^2 \right\rangle$ ) caused by turbulence and bed geometry, which contributes to the vertical momentum. This fact shows that among all components of form-induced stresses and Reynolds stresses, only $\langle \overline{w'^2} \rangle$ and $\langle \tilde{w}^2 \rangle$ are important in vertical momentum transport. In several studies, it is assumed that vertical velocity fluctuations support sediment suspension [11, 48, 49]. Bagnold [11] stated that the asymmetric probability density of vertical velocity causes net vertical momentum flux which keeps particles in suspension despite the influence of gravity. Also, vertical turbulent and form-induced momentum fluxes in Eq. 2 are always positive. However, depending on the sign of $w^{'}$ and $\tilde{w}$, they can be in upward or downward directions. To examine intensity and size of positive and negative vertical velocity fluctuations in time and space, conditional analysis must be implemented.

Following Bagnold's hypothesis, there have been attempts to study sediment transport in association with vertical velocity statistics [48, 49]. Leeder [48] and Wei & Willmarth[49] have correlated the transport of fine sediments to point measurements of vertical velocity. Wei and Willmarth [28] proposed a conditional analysis method to study the statistical characteristics of the vertical velocity measured point by point. In this method, as shown in Figure 1a, the intervals of positive vertical velocity ($\Delta t_+$) are separated from the intervals of negative vertical velocity ($\Delta t_-$). Accordingly, the total duration of measurement ($T$) comprises the total duration of positive vertical velocity ($T_+$) and negative vertical velocity ($T_-$) i.e. $T = T_+ + T_-$. .In this case, upward and downward turbulent vertical momentum fluxes can be defined as [28]:

$$\overline{w'^2}_+ = \frac{1}{T_+} \sum {w'^2_+}^i \Delta t^i_+ \tag{3}$$

$$\overline{w'^2}_- = \frac{1}{T_-} \sum {w'^2_-}^i \Delta t^i_- \tag{4}$$

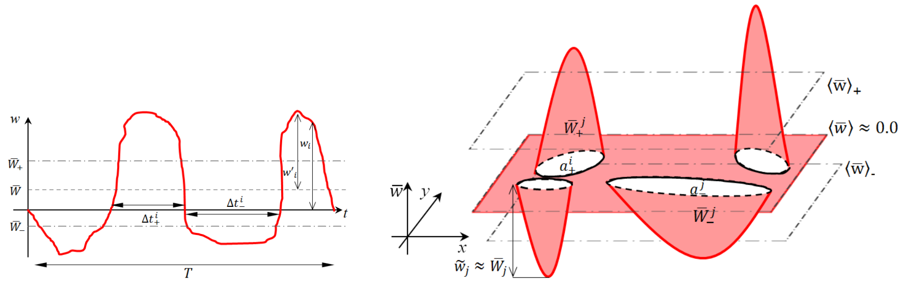

*(a)* *(b)*

Figure 1: Schematic view of (a) vertical velocity signal with Wei and Willmarth's [28] parameters (b) spatial mean vertical velocity distribution with parameters used in extended Wei and Willmarth's [28] method.

where $\overline{w'^2}_+$ and $\overline{w'^2}_-$ are, respectively, upward and downward turbulent momentum fluxes and $w'^{2\,i}_-$ and $w'^{2\,i}_+$ are respectively second power of instantaneous negative and positive vertical velocity fluctuations. Thus, net vertical turbulent momentum flux (upward turbulent momentum flux minus downward turbulent momentum flux) is expressed as [28]:

$$\overline{w'^2}^{NF} = (T_+\overline{w'^2_+} - T_-\overline{w'^2_-})/T \qquad (5)$$

Note that, in theory, Eq. 3, 4 and 5 are conceptually referred to a continuum time signal. However, during experimental measurements, continuous velocity fluctuations above measurement frequency can not be resolved. So, $\Delta t^i_+$, $\Delta t^i_-$ are obtained from discrete values and the aforementioned equations should be written for discrete sampled data. In the present study, In contrast to the measurements of vertical velocity above a flat plate (study of Wei & Willmarth [28]), roughness elements cause spatial variation of mean vertical velocity near the bed. The mean vertical velocity, as shown in Figure 1a, $\overline{w}$ is not necessarily equal to zero and should be subtracted before estimation of momentum flux (Eq.3 and Eq.4). Spatial variation of mean vertical velocity also causes vertical form-induced stress which contributes to vertical momentum flux in addition to turbulent momentum flux. In fact, referring to Eq. 2, net vertical momentum flux can be given by the turbulent fluctuations term($\langle\overline{w'^2}\rangle$) and form-induced fluctuations ($\langle\tilde{w}^2\rangle$). This demonstrates that, based on Eq. 2, conditional analysis of vertical turbulent momentum flux should be supplemented with spatial averaging. Therefore, to study total net momentum flux (turbulent momentum flux plus form-induced momentum flux), the method of Wei and Willmarth should be extended by considering the double averaging method. Overall turbulent upward and downward momentum fluxes ($\langle\overline{w'^2}\rangle_+$,$\langle\overline{w'^2}\rangle_-$) are defined as:

$$\left\langle \overline{w'^2}_+ \right\rangle = \frac{1}{A}\sum \overline{w'^2}^j_+ a^j \tag{6}$$

$$\left\langle \overline{w'^2}_- \right\rangle = \frac{1}{A}\sum \overline{w'^2}^j_- a^j \tag{7}$$

where $A$ is the total area of the averaging domain, $a^j$ is the area which is attributed to the measurement at point j, $\overline{w'^2}_+^{\,j}$ and $\overline{w'^2}_-^{\,j}$ are vertical turbulent momentum flux which are attributed to the positive and negative time-averaged vertical velocity ($\overline{w}_-^j$ and $\overline{w}_+^j$), respectively. Moreover, The subscript $j$ represents the $j^{th}$ time-averaged data sample in the spatial domain which is different from subscript $i$ used in the time-dependent data record.This method of spatial averaging is consistent with a method used by Nikora et al. [39] which is known as intrinsic spatial averaging. The results obtained from Eq. 6 and Eq. 7 mark the fractional contribution of the double-averaged turbulent momentum flux in the upward and downward directions.

To extend this conditional analysis in space, as shown in Figure 1b, areas with positive contributions to $\overline{w}$ ($a_+^j$) should be distinguished from areas with negative contributions ($a_-^j$).~~The subscript $j$ represents the $j^{th}$ time-averaged data sample in the spatial domain which is different from subscript $i$ used in the time-dependent data record.~~ $a_+^j$ and $a_-^j$ are also obtained from discrete sample values, although, similar to the time signal, conceptually they are referred to as a continuous signal in space. Consequently, total measurement area ($A$) is divided into the area with positive time-averaged vertical velocity ($A_+$) and the area with negative time-averaged vertical velocity ($A_-$) i.e. $A = A_+ + A_-$. ~~We should~~

~~note that, in order to satisfy continuity, double-averaged vertical velocity should be zero ($\langle \overline{w} \rangle = 0$) and there should not be any difference between form-induced vertical velocity and time-averaged vertical velocity at each point ($\bar{w} = \tilde{w}$).~~ Similar analysis can be also applied to double-averaged vertical form-induced momentum flux. Similar to the explained conditional analysis for turbulent vertical momentum flux, positive and negative vertical form-induced momentum fluxes are also defined as:

$$\left\langle \tilde{w}^2 \right\rangle_+ = \frac{1}{A_+} \sum \left(\tilde{w}_+^2\right)^j a_+^j \tag{8}$$

$$\left\langle \tilde{w}^2 \right\rangle_- = \frac{1}{A_-} \sum \left(\tilde{w}_-^2\right)^j a_-^j \tag{9}$$

where $\tilde{w}$ is velocity fluctuation respect to double-averaged vertical velocity ($\langle \overline{w} \rangle$). Analogous to what is explained for turbulent net momentum flux due to fluctuations in time (Eq. 5), net momentum flux (upward flux minus downward flux) due to spatial variation is expressed as:

$$\left\langle \tilde{w}^2 \right\rangle^{NF} = (A_+ \langle \tilde{w}^2 \rangle_+ - A_- \langle \tilde{w}^2 \rangle_-)/A \tag{10}$$

Finally, to estimate total net vertical momentum flux, net vertical momentum flux due to spatial fluctuations ($\langle \tilde{w}^2 \rangle^{NF}$) should be accumulated with spatial averaged of net vertical momentum flux due to time fluctuations $\left\langle \overline{w'^2}^{NF} \right\rangle$ which can be expressed as:

$$\left\langle \overline{w'^2}^{NF} \right\rangle = \frac{1}{A} \sum \overline{w'^2}^{NF^j} a^j \tag{11}$$

So, the total net vertical momentum flux ($TNWF$) is:

$$TNWF = \left\langle \overline{w'^2}^{NF} \right\rangle + \left\langle \tilde{w}^2 \right\rangle^{NF} \tag{12}$$

Previous studies have shown that the upward momentum flux in channel flow is related to the bursting process [15, 27, 28]. From conventional long term averaging of the data, it is not possible to reveal any information about the bursting process [17]. To properly describe coherent structures such as the bursting process, different conditional sampling methods have been developed [17, 50, 51]. The most common conditional sampling method for detection of the bursting process is known as the quadrant analysis [52]. Quadrant analysis is a method based on the premise that correlation of $u'$ and $w'$ is related to the bursting events [17]. Ejection ($u' < 0, w' > 0$) is the quadrant 2 ($Q_2$) and sweep ($u' > 0, w' < 0$) is the quadrant 4 ($Q_4$) [17, 52]. Quadrants 1 and 3 ($Q_1, Q_3$) are outward and inward interactions, respectively [17]. Generally, in quadrant analysis only intense fluctuations should be considered. Indeed, small fluctuations cancel each other out and are not important in the momentum flux process [53]. To eliminate small instantaneous fluctuations, it is assumed that intense instantaneous fluctuations should be greater than a certain threshold. As a first approximation, this statistical threshold was a portion of Reynolds shear stress ($\varkappa\overline{u'w'}$, where $\varkappa$ is a constant coefficient known as *'hole size'*) [54]. Later, Lu and Willmarth [52] and Bogard and Tiederman [55] compared instantaneous fluctuation ($u'(t)w'(t)$) with turbulence intensities in streamwise and vertical directions ($\varkappa\sigma_u\sigma_w$). Recently, Narasimha et al. [53] suggested root mean square of instantaneous $u'(t)w'(t)$ fluctuations ($\varkappa\sigma_{u'w'}$) as the threshold. The fraction of fluctuations which is discarded in quadrant analysis is also dependent on the value of coefficient $\varkappa$, selected as hole size. In the present study, we follow the threshold suggested by Bogard and Tiederman [55] ($\varkappa\sigma_u\sigma_w$) with hole size equal to 1.0 ($\varkappa = 1.0$). This threshold and hole size have been widely used in clear water open channel flows [30, 56].

According to the quadrant analysis, the fractional contributions to different Reynolds stress components from each quadrant can be estimated by:

$$(\overline{u'_m u'_n})_i = \lim_{T\to\infty} \frac{1}{T} \int_0^T u'_m\,(t)\,u'_n(t)\xi_i dt \tag{13}$$

where $(\overline{u'_m u'_n})_i$ is the fractional contribution of quadrant $i$ to specific component of Reynolds stress tensor $(\overline{u'_m u'_n}$ where $m$ and $n$ are velocity tensor notation) and $\xi_i$ is the detecting function defined as follow:

$$\xi_i = \begin{cases} 1.0 & u^{'}(t)\, w^{'}(t) > \sigma_u \sigma_w \; and \\ & located \; in \; i^{th} \; quadrant \\ & \\ 0.0 & elsewhere \end{cases} \tag{14}$$

## 3. Experimental Set-Up

The experiments were conducted in a tilting, water recirculating flume with a rectangular cross section (width $0.4m$; depth $0.4m$; length $6m$) at the Hydraulics laboratory, University of Trento. The discharge at the flume inlet was controlled by an inverter for pump speed regulation and measured by an electromagnetic flow-meter. Free surface profiles were measured by an ultrasonic distance transducer. The flume bed was covered by a layer of gravel $20cm$ thick. Gravel material was spread uniformly on the channel bottom to create a homogeneous gravel-bed layer (Figure 2a). The bed material had a median diameter ($D_{50}$) of $22mm$ and $D_{90} = 29mm$ (where $D_{90}$ is the particle diameter for which 90% is finner). In this study, the standard right-handed $x, y, z$ coordinate system is used. $x-$coordinate is in the main flow direction, positive from upstream to downstream. The $z-$coordinate is in the vertical direction (perpendicular to the streamwise direction) with reference to ~~the bed material (gravel) crest ($z_c$)~~ and is positive in the upward direction. The $y-$coordinate is in the spanwise direction and is positive from the right to the left wall.

The topography of bed elevations was measured by a M5L/200 laser scanner, covering a bed region above which velocity measurements were made. The standard deviation of bed elevations ($\sigma_l$) which is a representative roughness scale (sensu Nikora et al. [57]) was estimated as $6.1mm$.

In Figure 2b the roughness geometry function $\Phi$ is shown~~, which is defined as the ratio of the area occupied by fluid to the total area of the averaging domain~~

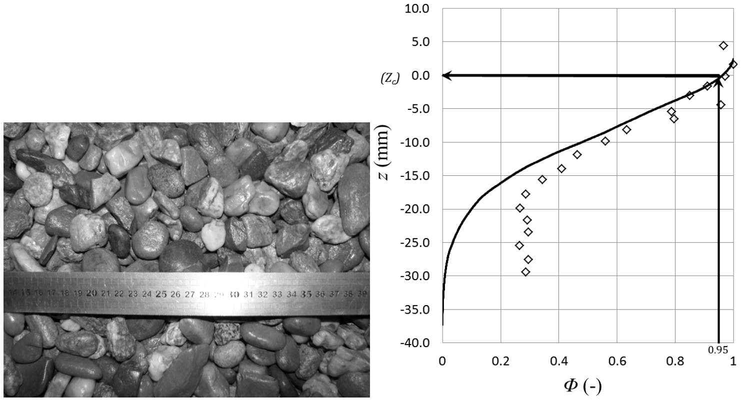

*(a)* *(b)*

Figure 2: (a) photograph of the gravel bed (b) roughness geometry function $\Phi$ as measured with water displacement method ($\diamond$) and with digital elevation method (black line).

~~that includes, below roughness crests, the gravel particles.~~ The roughness geometry function was evaluated by two different methods: (1) elevation distribution method; and (2) water displacement method Aberle [58]. The first method is based on the digital elevation model of the bed topography measured by laser scanner. In the second method, water was filled stepwise into the gravel bed and $\Phi$ was calculated from the volume of the added water and the associated increment of the water levels after Aberle [58]. The mean bed level $Z_m$ was $12.7mm$ lower than the gravel crest level $Z_c$, defined as the elevation corresponding to 95% of cumulative frequency of measured bed surface elevations. This $Z_c$ level is defined as the origin of the vertical coordinate $z$. More information and discussion concerning statistical charateristics of gravel bed in present study can be found in Mohajeri et al. [59].

During the measurements, three different hydraulic scenarios (named Run (I), Run (II) and Run (III)) were studied with different discharges and water depths. However, to simplify the problem, Froude number ($Fr$) intentionally maintains almost constant value which is similar to the observed Froude number in shallow natural gravel bed flow [60]. The experimental conditions for the three sets of laboratory measurements are reported in Table 1. The values of shear velocity in Table 1 are obtained from extrapolation of the double averaged Reynolds shear stress profile to the gravel crest. Dimensionless vertical roughness length scale $\Delta^+ = u_*\sigma_l/\nu$ (where $\nu$ is water kinematic viscosity, and $u_*$ is the shear velocity) much larger than 5 which is an estimate of dimensionless viscous sublayer thickness [61]. This means that the studied flows exhibited a hydraulically-rough bed condition. Relative submergence ($H_o/\sigma_l$ where $H_o = H + \sigma_l$ and $H$ is water depth) spanned from 7.5 to 10.8 showing that all three experimental flows can be defined as flows with small relative submergence [62, 63]. The entrance length for fully developed conditions ($X_L$) was estimated with the Nikora et al. [64] formula (see Table 1).

Table 1: Hydraulic conditions of the three laboratory experiments.

| - | **Run (I)** | **Run (II)** | **Run (III)** |
|---|---|---|---|
| $H(m)$ | 0.04 | 0.052 | 0.06 |
| $S(-)$ | 0.0028 | 0.0026 | 0.0029 |
| $Fr(-)$ | 0.51 | 0.47 | 0.51 |
| $Re_H \times 10^3(-)$ | 12.75 | 17.63 | 23.32 |
| $B/H(-)$ | 10 | 7.7 | 6.7 |
| $Q(10^{-3}m^3/s)$ | 5.1 | 7.05 | 9.33 |
| $\Delta^+(-)$ | 170 | 201 | 250 |
| $X_L(m)$ | 1.37 | 1.61 | 1.74 |
| $H_o/\sigma_l$ | 7.5 | 9.5 | 10.8 |
| $u_*(m/s)$ | 0.028 | 0.033 | 0.041 |
| $U_{ave}(m/s)$ | 0.32 | 0.34 | 0.39 |

$S$: channel slope, $Fr = u_{ave}/\sqrt{gH}$: where $g$ is acceleration of gravity, $Re_H = u_{ave} * H/\nu$: Reynolds number, $Q$: water discharge

Measurements were performed in a flow region at least $150mm$ from both side walls at a distance of $3.3m$ from the entrance of the channel, where the velocity profile is fully developed while the effects of the downstream weir remain negligible. The flow fields were measured in two series of Particle Image Velocimetry (PIV) on the vertical planes and the horizontal layer. In the first series of experiments, stereo-PIV was applied to measure three components of velocity (streamwise $u$, spanwise $v$ and vertical component $w$) at an $x - y$ horizontal layer located $1mm$ above the gravel crests. In the second series of experiments, two dimensional PIV was employed in three vertical planes ($x - z$ plane) located especially at the centreline, $50mm$ to the left and $50mm$ to the right of the channel centre line. The camera and laser were high-speed Fastcam X 1024 PCI Photron and Nd:Yag in continuous mode, respectively. The tracers used in all the experiments were sieved pollen particles with a diameter ranging from 0.075 to $0.125mm$ and a density of $1.07gr/cm^3$. The size of the measurement region was equal to $1024 \times 512px^2 \approx 128 \times 64mm^2$ in the vertical planes and $1024 \times 1024px^2 \approx 140 \times 140mm^2$ in the horizontal layer. For each PIV measurement, vertical planes in total cover at least 12 gravel bed particles ($D_{50}$) along x-direction. The measurement sampling frequency was $500Hz$ and the flow was sampled for 38.4 and 13 seconds in each vertical plane and horizontal layer. Cooper and Tait [65] studied the effect of sampling duration on velocity measurement over gravel beds and a comparison with the present study shows that measurement duration in vertical planes is long enough to ensure statistical convergence of the measured flow field. Despite short measurement duration in the horizontal layers for obtaining reliable statistics, it seems that the duration is long enough for our analyses as its spatial equivalent exceeds 60 flow depths assuming Taylor's frozen turbulence hypothesis is valid [61]. In addition, the sampling errors were calculated based on a 95% confidence interval and Normal distribution [66] and are reported in Table 2.

Image analysis and processing were performed by PIVDEF software (CNR-INSEAN) [67]. To reduce the effects of laser flare, the minimum value of image intensity for each pixel was subtracted from the PIV recording. The flow field was reconstructed by iterative cross-correlation method with the smallest interrogation size equal to $32 \times 16$ (75% overlapped) in the vertical plane and $64 \times 64$ to $28 \times 28$ zero padded algorithm (50% overlapped) in the horizontal layer by applying windows deformation and subpixel refinement [68]. Finally, a median filter was applied to reduce the number of spurious vectors [69]. The final vector spacing was approximately $1mm$ in both the horizontal layer and vertical planes. In the horizontal layer, the 2D-3C reconstruction was performed using

Table 2: 95% relative sampling errors of turbulence parameters.

| | Vertical Planes (%) | | | Horizontal Layer (%) | | |
|---|---|---|---|---|---|---|
| | Run (I) | Run (II) | Run (III) | Run (I) | Run (II) | Run (III) |
| $\overline{w}$ | 28.14 | 24.41 | 30.36 | 15.91 | 15.28 | 29.87 |
| $-\overline{w'^2}$ | 1.96 | 2.34 | 2.22 | 4.88 | 5.24 | 4.88 |
| $-\overline{u'w'}$ | 0.43 | 0.53 | 0.51 | 0.75 | 1.05 | 0.89 |

Soloff polynomial algorithm 332 degree [70].

It has been shown that if the ratio of particle-image diameter to the size of a Charge-Coupled Device (CCD) pixel on the photograph is larger than 3-4, the uncertainty of the measurement is equal to one-tenth to one-twentieth of the particle diameter [71]. This condition was satisfied in all PIV measurements. More information concerning experimental arrangement and conditions are available in Mohajeri [72].

## 4. Results

### 4.1. Reynolds stresses

As we plan to conditionally analyse Reynolds stresses, it would be useful to start with demonstrating profiles of $\langle\overline{u'w'}\rangle$ and $\langle\overline{w'^2}\rangle$. The profiles of the non-dimensional spatially-averaged Reynolds shear stress ($\langle\overline{u'w'}\rangle/u_*^2$) together with the form-induced component ($\langle\tilde{u}\tilde{w}\rangle/u_*^2$) for all three runs are given in Figure 3a. Profiles of $\langle\overline{u'w'}\rangle/u_*^2$ increase linearly toward the bed and reach the maximum almost at the level of of the crest of the gravel particles. Below the crest, rapid reduction was observed. On the other hand, below the crest, profiles of $\langle\tilde{u}\tilde{w}\rangle/u_*^2$ increase significantly. Profiles of $\langle\tilde{u}\tilde{w}\rangle/u_*^2$ and $\langle\overline{u'w'}\rangle/u_*^2$ obtained from this study are in conformity with those reported by Nikora et al. [39], Manes et al. [63], Mignot et al. [51] and Dey and ~~Day~~Das[73]. From Figure 3a, it is clear that the values of $\langle\tilde{u}\tilde{w}\rangle/u_*^2$ vary from $-0.05$ to 0.22.~~ and this agrees with the observations of Manes et al. [63]. However,~~ Values of $\langle\tilde{u}\tilde{w}\rangle/u_*^2$ in Manes et al. [63] range from 0.00 to 0.5 which is wider than the the range of $\langle\tilde{u}\tilde{w}\rangle/u_*^2$ in present study. Instead, Nikora et al. [39] found similar values of $\langle\tilde{u}\tilde{w}\rangle/u_*^2$

(ranges from 0.0 to 0.2).

Profiles of non-dimensional spatially averaged vertical momentum flux ($\langle\overline{w'^2}\rangle/u_*^2$) and vertical form induced momentum flux ($\langle\tilde{w}^2\rangle/u_*^2$) for all three runs are reported in Figure 3b. Above the gravel crests, profiles of $\langle\tilde{w}^2\rangle/u_*^2$ increase with a decrease in $z/H$ and reach a maximum near the level of the crests of the gravel particles. Below the crest of the gravel particles, $\langle\tilde{w}^2\rangle/u_*^2$ rapidly reduces. This observation is consistent with those reported earlier by many researchers [39, 63, 73] with the maximum value of $\langle\tilde{w}^2\rangle/u_*^2$ changing from 0.9 to 1.2, depending on the relative submergence. Manes et al. [63] report a maximum value of 1.0, while Dey and Das [73] observed a smaller value (0.7) and Nikora et al. [39] found a higher value (1.2). Profiles of the three runs are clearly separated over the whole flow depth, demonstrating higher vertical momentum flux for lower flow submergence. This observation differs from that reported by Grass [27] and Nezu and Nakagawa [17], who highlighted a tendency for the vertical turbulence intensity to increase in the near-bed region with increasing the roughness scale ($\Delta^+$). This discrepancy suggests that in our data set the turbulence structure has a greater dependence on flow submergence than on the bed roughness. However, the unambiguous separation of these two effects in our experiments was not possible. The analysis of the form-induced vertical momentum flux shows a strong increment near the crest of the gravel particles, while no sharp peaks for $\langle\tilde{w}\tilde{w}\rangle/u_*^2$ are visible. Form-induced vertical momentum flux assumes values at the gravel crests range between 0.05 and 0.15, similar to those obtained by Manes et al. [63] and by Dey and Das [73].

### *4.2. Examination of vertical momentum flux*

In previous studies, it has been observed that vertical velocity is positive in the upstream zone and negative in the downstream zone of roughness elements. As an example, Dancey et al. [74] found positive and negative vertical velocity, respectively, in the zones upstream and downstream of uniformly-distributed spheres. In the case of a random gravel bed, McLean and Nikora [41] also ob-

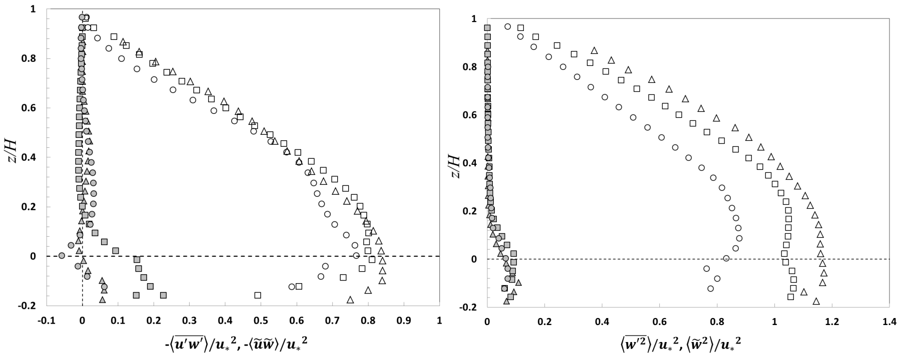

***(a)*** ***(b)***

Figure 3: (a) Spatially-averaged Reynolds shear stress (open symbols) and form-induced shear stress (filled symbols) profiles (b) Vertical profiles of spatially-averaged turbulent vertical momentum flux (open symbols) and form-induced vertical momentum flux (filled symbols); △ Run (I); □ Run (II) ○ Run (III).

served that the form-induced component of vertical velocity ($\tilde{w}$) is positive in the upstream zone and negative in the downstream zone. The spatial organization of near-bed vertical velocity observed in the present study follows this pattern. Figure 4 shows contour maps of the vertical velocity normalized with respect to $u_*$ in the vertical plane 1 (Figure 4a) and the horizontal layer (Figure 4b) for run (I). In Figure 4b, the red dashed line marks the position of the horizontal layer. Also, in Figure 4b, the red dashed lines mark the position of the vertical planes and the black shaded areas represent those parts of the bed topography which are higher than the mean value of the bed elevations (i.e. the gravel crests). In the near bed region, the bed topography is expected to show patches of positive and negative vertical velocity [74]. This is observed in present data for $z <\approx 2.5\sigma_l$ which corresponds to $z/H <\approx 0.35$ in Figure 4a. ~~In the near-bed region, shown in Figure 4a ($z \approx 2.5\sigma_l$ which corresponds to $z/H < 0.35$ in Figure 4a), the vertical velocity is heterogeneous with patches of high positive and negative values. In agreement with what has been observed in previous studies, the spatial variation of vertical velocity in both the vertical plane and horizontal layer are affected by the bed topography.~~ Furthermore, in

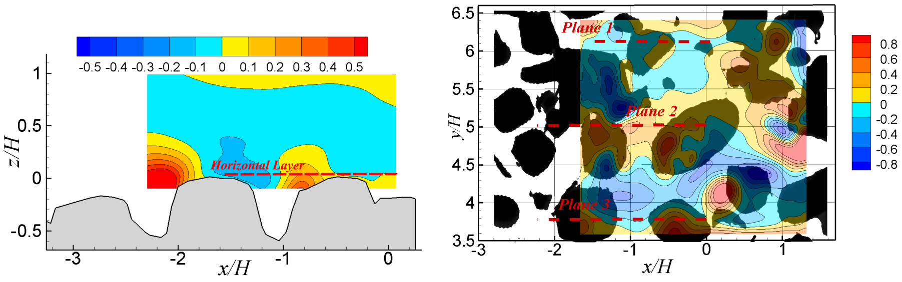

*(a)* *(b)*

Figure 4: Contour maps of non-dimensional vertical velocity ($\overline{w}/u_*$) (a) in vertical plane 1 (b) in horizontal layer just above the crest for Run (I), flow from left to right. (c) profiles of double-averaged vertical velocity normalized with mean streamwise velocity ($\langle\overline{w}\rangle/U_{ave}$).

Figures 4a and 4b at the upstream face of the gravel crests, flow tends to be diverted upwards, while at the downstream face, downward flow occurs. Far from the bed ($z/H > 0.5$), vertical velocity values tend to be negligible, In agreement with what has been observed in previous studies.

Figure 5 displays the spatial pattern of Net Vertical Turbulent Momentum Flux $\overline{w'^2}^{NF}$ (see Eq. 5). The values are normalized with respect to $u_*^2$. Similar to the observed distribution of mean vertical velocity, Figure 5a shows that $\overline{w'^2}^{NF}$ in the vertical planes is mostly positive above the gravel crests. Referring to both contour maps (Figure 5a and 5b), it is observed that in the gravel crest region general negative values of $\overline{w'^2}^{NF}$ are located downstream of the gravels. Also, local positive maximum values of $\overline{w'^2}^{NF}$ are mostly found at the upstream side of the gravels. Below the gravel crests, negative values of $\overline{w'^2}^{NF}$ tend to slightly prevail. We have to bear in mind that by the definition of $\overline{w'^2}^{NF}$ (Eq. 5), positive values of $\overline{w'^2}^{NF}$ can be associated to corresponding positive or negative values of $\overline{w}$. Moreover, conformal to observations of Wei & Willmarth [28], values of $\overline{w'^2}^{NF}$ and $\overline{w}$ underline two different mechanisms of vertical momentum transfer: the former can gives reason of a vertical convective momentum transport, while the latter is responsible for turbulent vertical momentum transport. Therefore, looking at Figure 4 and 5, we can argue that far from the bed the vertical turbulent momentum flux is mainly positive and therefore it tends to maintain any sediment particle that is transported by the flow into suspension, while in this region vertical convective motion is negligible. Closer to the bed, at the gravel crest region, both convective and turbulent vertical momentum fluxes works "in phase", that are mainly upward directed at upstream face of gravel and downward directed at its downstream face. Moreover, going further below gravel crest region, net vertical turbulent momentum flux tend to be mainly downward directed, so turbulent upward transport of the particles lie in this region is quite difficult. ~~Figure 5 displays the spatial pattern of mean net vertical momentum flux (see Eq. 5) due to the turbulence. The values are normalized with respect to $u_*^2$. Similar to the observed distribution of mean vertical velocity, Figure 5a shows that $\overline{w'^2}^{NF}$ in the vertical planes is mostly positive above the gravel crests. Below the gravel crests there are some regions where negative values of $\overline{w'^2}^{NF}$ are found. Referring to both contour maps (Figure 5a and 5b) it is observed that in general negative values of $\overline{w'^2}^{NF}$ are located downstream of the gravels. Also, local positive maximum values of $\overline{w'^2}^{NF}$ are mostly found at the upstream side of the gravels.~~ In contrast to the findings of the present study, Dancey et al. [74] found that the turbulent velocity fluctuations, above roughness elements, give an overall upward directed momentum flux with maximum values registered at the "gap" between adjacent roughness elements and minimum values at the gravel crest region, both immediately downstream and upstream of it. They finally concluded that in the horizontal layer above roughness elements there are two counteracting effects on net vertical momentum fluxes: the mean (time-averaged) motion causes a downward directed flux, while the turbulent velocity fluctuations give an overall upward directed momentum flux. Contour maps of our data in Figure 5 show that turbulent velocity fluctuations do not necessarily contribute to upward movement and they can also cause downward movement. However, the overall trend of net vertical turbulent momentum flux near gravel particle crests can be better seen by the spatially averaged profiles of $\overline{w'^2}^{NF}$.

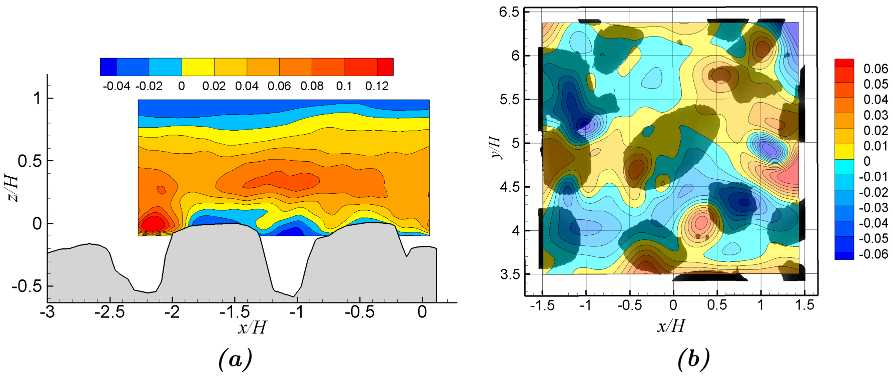

Figure 5: Contour maps of non-dimensional net vertical turbulent momentum flux ($\overline{w'^2}^{NF}/u_*^2$) (a) in vertical plane 1 (b) in horizontal layer 1mm above the crest in Run (I), flow from left to right.

To further explore vertical momentum flux, the double averaging method was applied to the turbulent momentum flux. In Figure 6, profiles of double-averaged upward and downward turbulent and form-induced momentum fluxes are shown. The values are made dimensionless with second power of the shear velocity. Both upward and downward turbulent momentum fluxes increase from the water surface toward the bed. Near the bed ($z/H < 0.4$ in Figure 6a and $z/H < 0.3$ in Figure 6b) both upward and downward turbulent momentum fluxes become almost constant, the maxima being located approximately at the gravel particle crests for upward momentum fluxes, while for the downward directed turbulent momentum fluxes the maxima tend to be located slightly below the level of the gravel crests. Below the gravel particle crests both upward and downward momentum fluxes attenuate abruptly. Note that in this region, attenuation of upward turbulent momentum flux seems to be faster than downward turbulent momentum flux. The overall impression is that the downward directed turbulent momentum fluxes affect a larger area between the gravels (interfacial sub-layer) than upward directed turbulent momentum fluxes. The form-induced upward and downward momentum fluxes are not noticeable far from the gravel bed. Near the bed $z/H < 0.1$, both $\langle \tilde{w}^2 \rangle_+ / u_*^2$ and $\langle \tilde{w}^2 \rangle_- / u_*^2$ become significant.

Around the gravel crests ($-0.1 < z/H < 0.1$), dimensionless form-induced upward and downward momentum fluxes are smaller than 0.2, while dimensionless upward and downward turbulent momentum fluxes are larger than 0.8. ~~This indicates that although both upward and downward form-induced momentum fluxes are not high; they are not completely negligible in comparison to upward and downward turbulent momentum fluxes.~~ In particular, focusing our attention on upward momentum flux, Figure 6a, we can recognize form induced contribution to upward motion represented by $\langle \tilde{w}^2 \rangle_+ / u_*^2$ which can be considered as the "convective" component to vertical momentum flux, is about 0.2, while the turbulent component, $\langle \overline{w'^2}_+ \rangle / u_*^2$ ranges between 1.1 and 0.5 in the same region. Therefore, we can argue that in the region $-0.1 < z/H < 0.1$, the contribution of the form induced stresses to the potential fine sediment entrainment and resuspension is not negligible with respect to the turbulent contribution (see Eq. 2). As far as the downward vertical momentum flux is concerned (Figure 6b), the situation is a bit different. The turbulent component $\langle \overline{w'^2}_- \rangle / u_*^2$ is more vigorous than the corresponding upward component and tend to persists more in depths beneath the gravel crest, assuming values ranging between 0.7 and 1. At the same time, the form induced component $\langle \tilde{w}^2 \rangle_- / u_*^2$ hardly assumes values higher than 0.1. Therefore, in the region immediately below gravel crests there is an "asymmetric" behavior of upward and downward turbulent events that contribute to vertical momentum budget (Eq. 2), and so to fine sediment particle transport. This makes the upward dispersive component of vertical momentum flux not negligible compared to the upward turbulent component, while in the downward component flows this is not so true. This circumstance call for a deeper analysis of the turbulent structure of the flow field, especially at the near bed region, that will be performed in the next paragraph through a quadrant analysis of the measured velocity field.

The profiles of double-averaged vertical net turbulent momentum flux ($\langle \overline{w'^2}^{NF} \rangle / u_*^2$) are shown in Figure 7a. The profiles of all three runs have maximum positive values at the middle of the water column ($z/H \approx 0.45$). The values decline from $z/H \approx 0.45$ to the water surface where $\langle \overline{w'^2}^{NF} \rangle / u_*^2$ is approximately equal

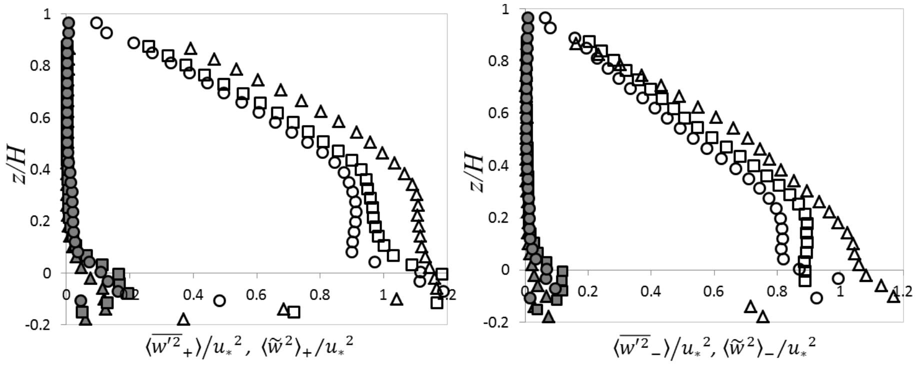

*(a)* *(b)*

Figure 6: Profiles of double-averaged (a) upward momentum flux profiles (b) downward momentum flux profiles (open symbols due to the turbulence; filled symbols due to the spatial fluctuations).

to zero. From $z/H \approx 0.45$ toward the gravel bed, profiles of $\langle \overline{w'^2}^{NF} \rangle / u_*^2$ reduce and below the gravel particle crests ($z/H < 0.0$), the values are negative. The profiles of net vertical turbulent momentum fluxes described in the present study differ slightly from those observed for smooth beds, especially in the near-bed region. For smooth beds, profiles of net vertical turbulent momentum flux are positive almost everywhere, except in $10 < z_+ < 30$ ($z_+ = (zu_*)/\nu$) where the values of $\overline{w'^2}^{NF}$ become negative [28]. This region ($10 < z_+ < 30$) almost overlaps with the buffer layer. Results from the present study show that over a rough bed, net vertical turbulent momentum flux is positive in the outer part of the roughness layer (almost overlapping with the form-induced sub-layer). However, in the inner part of the roughness layer (almost overlapping with the interfacial sub-layer) net vertical turbulent momentum flux is negative. These results are consistent with the description of the near-bed large scale coherent structures dynamics given e.g. by Detert et al. [21] and Migniot et al. [51] for gravel bed flows. At the near-bed region (typically $z/H < 0.4$) sweep-like flow structures over-roll and interact with low momentum ejection-like flow which causes high turbulence kinetic energy production and transport in and from the near bed region.

In Figure 7b, the net vertical momentum flux due to spatial heterogeneity (net form induced momentum flux) of vertical velocity ($\langle \tilde{w}^2 \rangle^{NF}/u_*^2$) is shown. The values are negligible above the gravel crests, but near the bed ($z/H < 0.1$), they have an incremental trend to reach positive values. Comparison of Figure 7a and 7b shows that $\langle \tilde{w}^2 \rangle^{NF}/u_*^2$ and $\langle \overline{w'^2}^{NF} \rangle/u_*^2$ are nearly at the same order of magnitude. It is interesting since, as highlighted, in Figure 6, upward and downward form-induced momentum fluxes are significantly smaller than upward and downward turbulent momentum fluxes, while their net effects reach approximately the same order of magnitude with opposite signs. Below the gravel particle crests, net turbulent and form-induced momentum fluxes present opposite behaviours. Specifically, while near the gravel bed $\langle \tilde{w}^2 \rangle^{NF}/u_*^2$ is directed upwards, the $\langle \overline{w'^2}^{NF} \rangle/u_*^2$ is negative (tendency to transport mass downward with turbulent momentum flux and upward with form-induced momentum flux).

As explained in the Theoretical Background, in theory, double-averaged vertical velocity $\langle \overline{w} \rangle$ must be equal to zero. However, our experimental results show that in Run I and II below gravel particle crest, in some points there is not negligible positive double-averaged vertical velocity. Non-zero values of $\langle \overline{w} \rangle$ could be the result of the measurement uncertainty or properties of spatial averaging in the present study. Indeed, the form induced components are sensitive to both the minimum required size of spatial averaging and to the density of measurements [65]. The non-zero vertical double-averaged velocity can affect the results shown in Figure 7b. However, we do not believe that the trend of positive net vertical form-induced momentum flux below the gravel crests is strongly affected by $\langle \overline{w} \rangle \neq 0$. As a matter of a fact, in Run III, below gravel particle crest level with $\langle \overline{w} \rangle \approx 0$, the values of net vertical form-induced momentum fluxes are still positive (Figure 7b) and are still the same order of magnitude as the net vertical turbulent momentum flux.

To better compare the contribution of $\langle \tilde{w}^2 \rangle^{NF}$ and $\langle \overline{w'^2}^{NF} \rangle$ to vertical momentum flux, the total vertical net momentum flux ($TNWF$), obtained from Eq. 12, is presented in Figure 7c. At the near-bed region ($z/H < 0.1$), the simul-

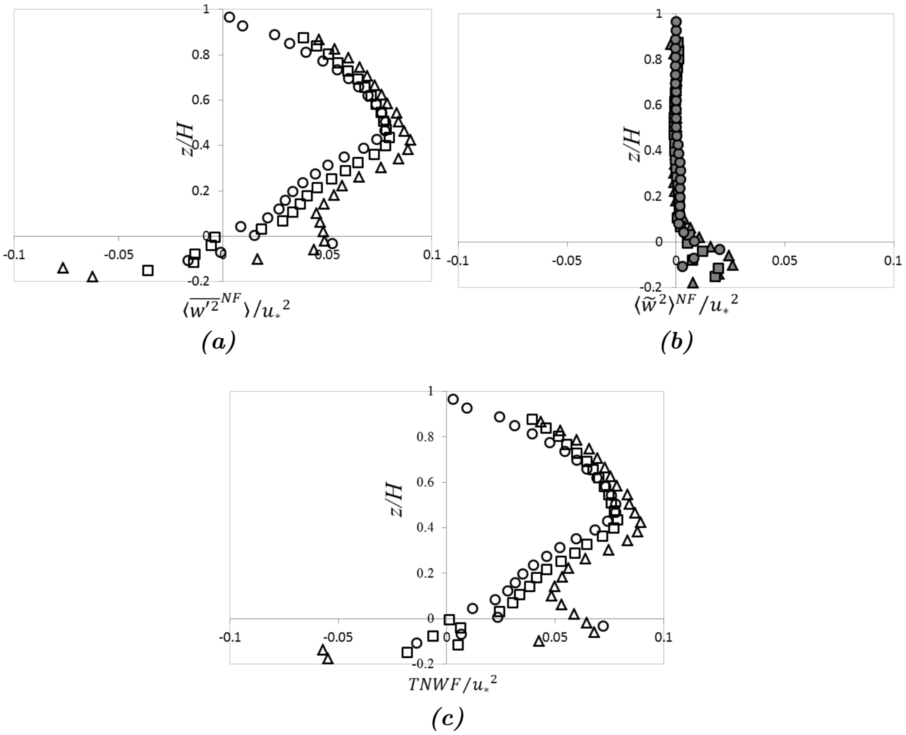

*(a)* *(b)*

*(c)*

Figure 7: Profiles of (a) double-averaged vertical net momentum flux profiles ($\langle \overline{w'^2}^{NF} \rangle / u_*^2$) (open symbols) (b) vertical net momentum flux due to spatial heterogeneity ($\langle \tilde{w}^2 \rangle^{NF} / u_*^2$) (filled symbols) (c) total net vertical momentum flux ($TNWF/u_*^2$) (open symbols) for three Runs; △ Run (I); □ Run (II) ○ Run (III).

taneous effects of net momentum flux due to both time and space fluctuations is noticeable. It seems that in a level below the gravel crests ($z/H < -0.1$) the values of form-induced momentum fluxes are smaller than the values of vertical turbulent momentum flux and so total vertical net momentum flux is negative.

### *4.3. Quadrant analysis*

The analysis of the vertical velocity component, both in time and space, has allowed us to depict those characteristics of the turbulent flow field which are important in the vertical momentum transport equation. In order to relate the features of the vertical momentum fluxes to the bursting process, quadrant analysis was undertaken and the results were compared to values reported in the literature. It is noteworthy that most of the published data refer to flows on smooth or rough beds at high submergence conditions ($H \gg \sigma_l$), therefore the spatial variations at the bed have not been analysed. Only the data of Hardy et al. [62], Dey and Das [73], Mignot et al. [51] and Sarkar and Dey [75] explicitly refer to quadrant analysis over very rough beds and consider the effect of spatial heterogeneity which characterizes the roughness layer. However, these studies consider flow with high relative submergence ($H/\sigma_l = 25.3$ in Dey and Das [73], $H_o/d_{50} = 21.9$ in Mignot et al. [51] and $H_o/\sigma_l = 25.6$ in Sarkar and Dey [75]), while present data concern flow at lower relative submergence ($H_o/\sigma_l = 7.5 \sim 10.8$ see Table 1).

In Figure 8, results of the quadrant analysis for Run (I) and in plane 1 are shown. In this Figure, contributions of each quadrant to Reynolds shear stress are normalized with respect to $u_*^2$. The data in Figure 8 refer to the hole size ($\chi$) equal to 1.0 (for more information, see Theoretical Background). In agreement with the data reported in the literature for smooth and rough bed flows [15, 17], the absolute values of the contributions from quadrants 2 (Figure 8b) and 4 (Figure 8d) are higher than the contributions from quadrants 1 (Figure 8b) and 3 (Figure 8c). For present study, in the near-bed region (below gravel crests to the level $z = 3\sigma_l$), all contour maps are heterogeneous. Hardy et al. [56] also found spatial variation of different quadrants at $z/H < 0.15$. The larger area affected by the bed topography in the present study ($z/H < 0.3$ in Figure 8b) can be ascribed to different configurations of bed topography and smaller relative submergence in this research. Additionally, there is experimental evidence that quadrant 2 events and its fractional contribution to Reynolds shear stress are predominant in the outer part of the near-bed region, while closer to the bed, quadrant 4 events tend to be prevalent [14, 15, 17, 27, 37, 76, 73, 51]. Similarly, Figures 8a and 8d clearly show that while quadrant 2 events are intense in the near-bed region and above gravel crests ($0.0 < z/H < 0.3$), quadrant 4 shows local peaks only in the gaps between gravel crests ($z/H < 0.0$) and suggest that

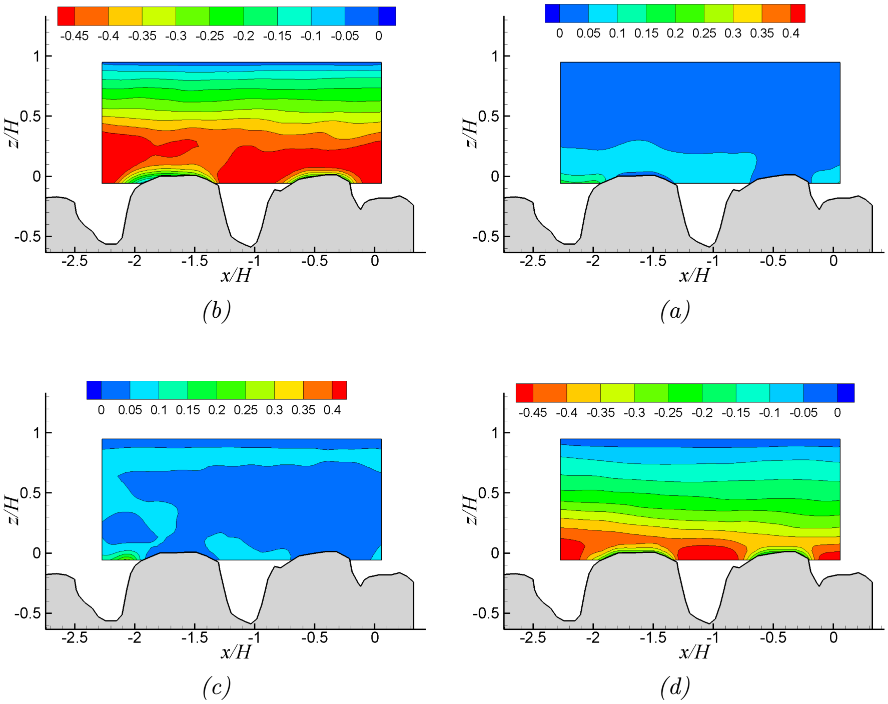

(b) (a)

(c) (d)

Figure 8: Contour map of non-dimensional Reynolds shear stress for different events $((\overline{u'w'})_i/u_*^2)$ with $\varkappa = 1.0$ in vertical plane 1 for Run (I), Plane 1; (a) quadrant 1, (b) quadrant 2, (c) quadrant 3, (d) quadrant 4.

the higher contribution of quadrant 4 takes place in the region below the gravel crests. To further investigate the spatial organisations of four quadrants with respect to bed topography, quadrant analysis was repeated for the horizontal layers. The results of quadrant analysis in horizontal layers show a correlation between the occurrence of quadrant 2 and 4 events and bed topography. As an example, the results of quadrant analysis in the horizontal layer and for Run (I) are shown in Figure 9. In all contour maps in Figure 9 (a: quadrant 1, b: quadrant 2, c: quadrant 3 and d: quadrant 4), locations of gravel crests are also shown in the background similar to the previous figures. These contour maps show that the fractional contribution of all quadrants $((\overline{u'w'})_i/u_*^2)$ varies spatially with respect to the bed topography. More precisely, quadrant 2 mostly occurs at the upstream side of the gravel particle crests, while quadrant 4 is more common at the downstream side of the gravel particle crests.

To further investigate the contribution of different quadrants to Reynolds shear stress for flow over rough beds, especially in the near-bed region, double averaging is commonly used [73, 51, 75]. The results from applying the double averaging method to the present quadrant analysis are shown in Figures 10a and 10b. To better observe the variation of quadrant analysis with the hole size ($\varkappa$), results of quadrant analysis without eliminating mild fluctuations ($\varkappa = 0.0$) are also reported (the red symbols refer to the quadrant analysis with $\varkappa = 0.0$ and black symbols refer to the quadrant analysis with $\varkappa = 1.0$). Analogous to previous studies [17, 51], fractional contributions of all quadrants reduce with increases in the hole size, while the shape of the profiles are approximatively similar for different hole size. The spatially-averaged contribution to Reynolds shear stress from quadrants 1 and 3 are weak (open symbols in Figure 10a and 10b); and the corresponding profiles slightly increase by moving from the free surface towards the bed and then decline below gravel particle crests, the maxima being located slightly below the level of the gravel crests. Similar results are also reported in previous studies [73, 51, 75].

As far as quadrant 2 events are concerned (filled symbols in Figure 10a), their values increase moving from the free surface toward the bed. In the central region of the flow field ($0.5 > z/H > 0.1$) the values are almost constant and they decrease moving toward the bed and below the crest level ($z/H < 0.1$). Maxima of the ejection quadrant 2 contribution profiles are located at about the gravel crest level. The profiles of quadrant 4 events show slightly different behaviour (filled symbols in Figure 10b). Moving from the free surface toward the bed, the profiles increase almost linearly. The linear increase of quadrant 4 profiles continue even below the gravel crests level leading to the maximum values being located at about $z/H \approx -0.1$. Below this position all three profiles decrease. The features of the profiles do not show a significant change with or without eliminating mild fluctuations ($\varkappa = 0.0$ or $\varkappa = 1.0$). Figure 10c and 10d show the double-averaged contributions of quadrants 2 and 4 to the tur-

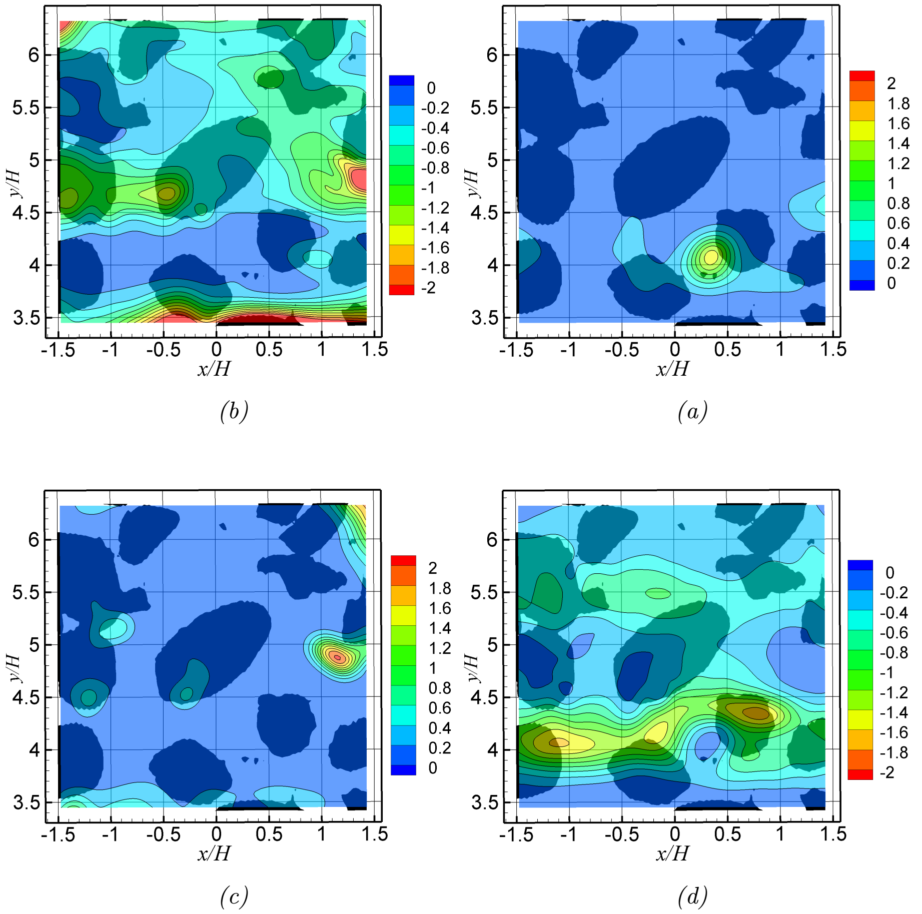

(b) (a)

(c) (d)

Figure 9: Contour map of non-dimensional Reynolds shear stress for different events ($(\overline{u'w'})_i/u_*^2$) with $\varkappa = 1.0$ in horizontal layer for Run (I); (a) quadrant 1, (b) quadrant 2, (c) quadrant 3, (d) quadrant 4.

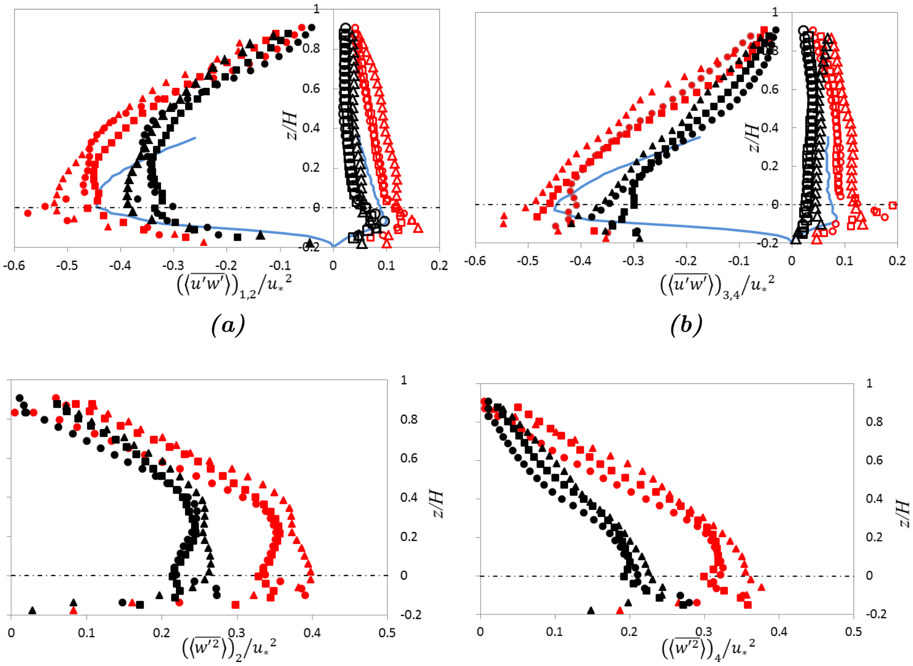

*(a)* *(b)*

*(c)* *(d)*

Figure 10: Double-averaged profiles of (a) $\langle\overline{u'w'}\rangle/u_*^2$ for quadrant 1 (open symbols) and 2 (filled symbols) (b) $\langle\overline{u'w'}\rangle/u_*^2$ for quadrant 3 (open symbols) and 4 (filled symbols)(c) $\langle\overline{w'^2}\rangle/u_*^2$ for quadrant 2 (d) $\langle\overline{w'^2}\rangle/u_*^2$ for quadrant 4 (△ Run (I); □ Run (II) ○ Run (III)) with $\varkappa = 0.0$ (red spots) and $\varkappa = 1.0$ (black spots); blue lines in (a) and (b) refers to Mignot et al. [51] with $\varkappa = 0.0$.

bulent vertical momentum flux, with and without hole size. It can be clearly recognized that, in the region above the gravel crests $z/H > 0$, the profiles conform to the corresponding Reynolds shear stress profiles for both quadrants 2 and 4 (Figure 10a and 10b). Below the gravel particle crests, some differences between Reynolds shear stress profiles and vertical turbulent momentum flux take place. Specifically, below the gravel particle crests, the contribution to the vertical momentum flux from quadrant 2 still increases and reaches a maximum, at about $z/H = -0.1$, below this level the contribution of quadrant 2 quickly declines. Therefore, one can argue that quadrant 4 events are more effective than quadrant 2 events in affecting the turbulent flow field below gravel crests. Also, at this level ($z/H = -0.1$), the contribution from quadrant 4 to turbulent vertical momentum flux reaches its maximum, similar to the profiles of quadrant 4 contributions to Reynolds shear stress (Figure 10b).

In order to better observe variations of quadrant 2 with respect to quadrant 4 along water depth, in Figure 11 the profiles of quadrant 2 and quadrant 4 ratio for Reynolds shear stress (Figure 11a) and vertical turbulent momentum flux (Figure 11b) are reported. In Figure 11a, it can be noted that in the interfacial sub-layer ($z < 0$) values of quadrant 2 are always lower than the corresponding quadrant 4 and also the decreasing trend of quadrant 2 is faster than that of quadrant 4. In contrast, above the gravel particle crests, the contribution of quadrant 2 is always higher than the corresponding quadrant 4.

Focusing the attention at the near-bed region, the results of this study confirm the findings of Mignot et al. [73] and Dey and Das [51] both for quadrant 2 and quadrant 4 profiles. In particular, all the experimental results confirm that the maximum contribution of quadrant 2 events is at the gravel crests level and below gravel crests there is a prevalence of quadrant 4 events over quadrant 2 events. Data comparison for the upper region (i.e. outer region) is not possible, because the measurement technique used by the authors (Acoustic Doppler Velocimetry probe) [73, 51, 75] does not allow measurements to span the region close to the free surface. Moreover, low aspect ratios in experimental measurements of Mignot et al. [73] and Dey and Das [51] speculate this

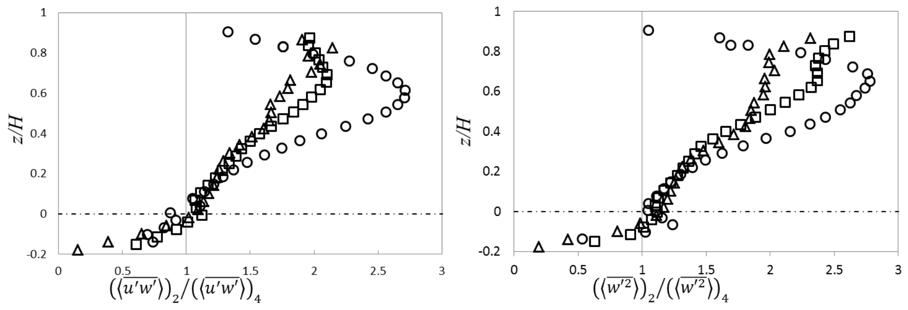

***(a)*** ***(b)***

Figure 11: Double-averaged profiles of the ratio between fractional contribution from quadrant 2 to quadrant 4 (a) for Reynolds shear stress $(\langle \overline{u'w'}\rangle_2/\langle \overline{u'w'}\rangle_4)$ (b) for vertical momentum flux $(\langle \overline{w'^2}\rangle_2/\langle \overline{w'^2}\rangle_4)$ with $\varkappa = 1.0$; △ Run (I); □ Run (II) ○ Run (III).

idea that the turbulent flow field in the outer region is affected by the presence of secondary currents and occurrence of dip phenomenon [17]. The profiles of $(\langle \overline{w'^2}\rangle)_2/(\langle \overline{w'^2}\rangle)_4$ ((Figure 11b)) show slightly different behaviour to the profiles of $(\langle \overline{u'w'}\rangle)_2/(\langle \overline{u'w'}\rangle)_4$, below gravel crests. In this region, there is a narrow band $(-0.1 < z/H < 0)$ where $(\langle \overline{w'^2}\rangle)_2/(\langle \overline{w'^2}\rangle)_4$ is still higher than unity, while the ratio of $(\langle \overline{u'w'}\rangle)_2/(\langle \overline{u'w'}\rangle)_4$ is lower than one.

## 5. Discussion

The analyses of present study focus on the vertical momentum flux. Many researchers believe that vertical momentum flux provide resistance oppose to settling tendency of a fine sediment grain and keep the sediment particles in suspension [11, 48, 77]. The percentage of upward and downward vertical velocity fluctuations in time and space is important for suspension [11]. In fact, the downward vertical velocity fluctuations support fine sediment settling, while upward vertical velocity fluctuations act to oppose the downward trajectory of a settling grain. To distinguish upward and downward vertical fluxes conditional analysis, as explained in the Theoretical Background, was used. Both vertical net turbulent and form-induced momentum flux were estimated and used to find the general trend of momentum transport in the vertical direction.

Moreover, to understand which turbulent motions are the main contributors to the net vertical turbulent momentum flux, the analysis of the quadrants is used. Originally, this analysis was developed for flat boundaries [54]. However, many researchers apply it to rough boundaries like gravel bed flows [75, 51, 76, 73]. There is a notable difference between application of quadrant analysis in flat and rough boundary conditions. According to the quadrants analysis, attribution of a value to a given quadrant is dependent on the orientation of the axes. Orientation is straightforward for fluxes over a flat bed, as $x-$ is oriented in the main flow (i.e. as the bed) and $z-$ is perpendicular to it. So, there would be $\overline{u} \neq 0$ and $\overline{w} = 0$, while in the case of a rough boundary, the orientation of the axes is not clear and consequently $\overline{u} \neq 0$ and $\overline{w} \neq 0$. In the present study, the quadrant analysis has been performed on spatially averaged quantities. Therefore, by definition, the spatially averaged vertical velocity component has to be equal to zero. This circumstance allows quadrant analysis to be performed regardless of the local orientation of time-averaged velocity, given that the spatially averaged vertical mean velocity, $\langle \overline{w} \rangle = 0$, does not contribute to any of the quadrants. This assumption allows the contribution of quadrants 2 and 4 to be considered as sweep and ejection events, respectively. More accurate analysis of sweep and ejection events in rough boundaries can be done through visualization of coherent structures [78, 79]. Results of coherent structures visualization can also give us the chance to control accuracy of the quadrant analysis results in rough boundaries but this matter needs to be better clarified in future studies. The small ratio of the vector spacing to the size of prevailing bed particles in our experiments provided the possibility to detect the disturbances of near-bed flow induced by bed topography.

Countour maps of net-vertical turbulent momentum flux in the horizontal layer (Figure 5b) show that protrusions of gravel crests tend to locally provoke flow diversions in upward and downward directions. These diversions are quite irregular and seem to be dependent on local orientation and shape of the pebbles that originate them. The profiles of double averaged vertical momentum flux (Figure 6 and 7) show that above gravel crests, the upward turbulent momentum flux tends to prevail, with a maximum located at about $z/H = 0.45$. At the gravel crest region ($0.1 < z/H < -0.1$), there is a substantial balance between upward and downward vertical momentum fluxes, while in the lower part of the roughness layer ($z/H < -0.1$) the downward turbulent momentum flux tends to prevail. Moreover, the dispersive component of vertical momentum flux is not negligible only at the roughness layer and upward directed. This means that while turbulence can sustain and maintain into suspension fine sediment particles above gravel crest, when particles are placed below gravel crest, turbulence can hardly pick-up and carry upwards it. On the other hand, this tendency to particle settling can be partially counterbalanced by convective upward motion represented by dispersive vertical momentum flux. With the aim to have a deeper insight about the features of vertical turbulent momentum flux, a quadrant analysis has been performed.

Contour maps of quadrant analysis in horizontal layer near gravel crests (Figure 9) reveal presence of spatial organizations, correlated with bed topography. Specifically, ejection events are common at the upstream side of gravel particles, while sweep generally happens at the downstream side of gravel particles. This observed interaction of bed topography and quadrant results is also reported by Hardy et al. [56]. They found alternating patterns of quadrants 2 and 4, respectively, at the upstream and downstream sides of gravel crests. Cooper and Tait [80] also reported the occurrence bursting events in the certain locations on their bed. However, they did not find any correlation between near-bed flow and bed topography probably because of insufficient spatial resolutionn (ratio of vector spacing in PIV measurement to $D_{50}$ of the bed materials) in their measurement (which is equal to 0.5) compared to the present study (which is equal to 0.05). Comparison of quadrant analysis and net-vertical turbulent momentum flux in the horizontal layer immediately above gravel crests suggests that net upward turbulent momentum flux, which is generally the result of ejection events, is mainly located at the upstream side of the particles, while net downward turbulent momentum flux, which is in general the result of sweep events, is mainly at the downstream side of the particles. ~~Comparison of quadrant analysis and net-vertical turbulent momentum flux in the horizontal layer suggests that net upward turbulent momentum flux at the upstream side of the particles is generally the result of ejection events, while net downward turbulent momentum flux at the downstream side of the particles is in general the result of sweep events.~~

Figure 12 is a schematic view of quadrant analysis and analysis of vertical velocity based on our experimental results shown in Figure 7a, 7b and 10. In this figure, it is possible to see the vertical momentum flux budget along the water depth and compare it with the occurrence of bursting process events. Three regions can be identified in the flow field: 1) *"Upper layer"* from free surface to about $z/h \approx 0.1$ where ejection events and related upward turbulent momentum flux prevail. In this layer form-induced vertical momentum flux is negligible. This layer can be divided in two parts. In the lower part, between $0.1 \approx z/H$ and the level of maximum total net turbulent momentum flux ($z/H \approx 0.45$), ejections and sweeps are still intense (see Figure 10). Therefore, this intense ejection event can entrain fine particles in the near gravel crests region, where sediment concentration is high [81], and bring them to the upper part of the flow, where sediment concentration is low [81]. In the upper part, between $z/H \approx 0.45$ and the free surface, the positive values of net turbulent vertical momentum flux result from a competing contribution of very weak ejection and sweep events (see Figure 10). So, in context of sediment transport, prevalence of this type of upward turbulent momentum flux could help to keep in suspension those particles which have already been suspended by the intense events coming from the near-bed region. 2) *"Lower layer"*, located below $z/H \approx -0.1$, in which sweep events are intense and are the main contributor both to Reynolds stress and to turbulent vertical momentum flux. Therefore, strong sweep events in this region can bring pulses of fast flowing water with relatively low sediment concentration down toward the bed. At the same time, the relatively high fractional contribution of quadrant 4 to Reynolds shear stress in this region can

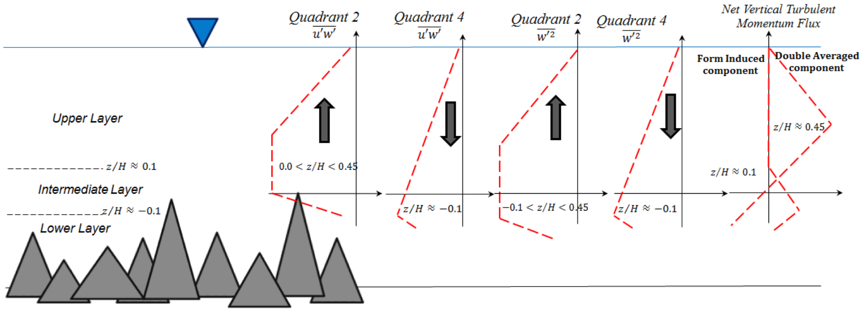

Figure 12: Schematic comparison of quadrant analysis and analysis of vertical velocity.

cause a potentially significant contribution to longitudinal sediment transport. 3) Near gravel crests, between upper and lower layers ($+0.1 < z/H < -0.1$), there is also an *"Intermediate layer"*, which is dominated by particularly intense ejection and sweep events. In this region, there is a substantial dynamic balance between quadrant 2 and 4 events to Reynolds shear stress contribution, with the higher contribution of the former occurring in the upper part of this layer ($z/H > 0.0$). In the upper part of this layer, values of both net turbulent and form-induced vertical momentum fluxes (Figures 7a and 7b) are positive and with the same order of magnitude. In the lower half of the intermediate layer ($0.0 > z/H > -0.1$), it is the contribution of sweep events to Reynolds shear stress that tends to be prevalent and the net vertical turbulent momentum flux is negative (downward directed) and is counterbalanced by the upward net form-induced momentum flux. It is important to highlight that despite the negative net vertical turbulent momentum flux in this region, the turbulent vertical momentum flux associated with ejections reaches its maximum values approximately at $z/H = -0.1$. This means that immediately below gravel crests, the vertical fluctuations induced by ejection events are more effective to produce vertical upward turbulent momentum than horizontal turbulent momentum. Therefore, it can be speculated that ejection events can lift up fine sediment particles from below the gravel crests, but their contribution to the longitudinal movement of particles in this region is negligible. Only after the fine particles have been lifted up above the level of the gravel crests by ejection can they be transported downstream by the longitudinal fluctuations.

Finally, it should be stressed that the analysis in the present study did not consider all the terms that appear in Eq. 2. Indeed, as discussed in the Theoretical Background, the last term in Eq. 2 ($\int_{z}^{z_c} \left[ \frac{1}{\Phi} \frac{\partial \Phi}{\partial z} (\rho \left\langle \overline{w'^2} \right\rangle + \rho \left\langle \tilde{w}^2 \right\rangle + \left\langle \overline{p} \right\rangle ) \right] dz$) which is caused by the variation of roughness geometry function in vertical direction has not been analysed. The main difficulty in the analysis of this term is to parametrize variation of bed geometry in the vertical direction.

## 6. Conclusions

This paper reports on an experimental investigation of the vertical momentum flux over an immobile gravel bed. Flow fields were measured with Stereo-PIV at the near-bed horizontal layer and Digital-PIV in the vertical planes covering three distinctly different hydraulic scenarios. The data were analysed through an extension of Wei & Willmarth's [28] method and quadrant analysis. In summary, the analysis of the data led to the following findings:

1. Spatial variation of vertical turbulent momentum flux is caused by bed topography. Net turbulent momentum flux occurs in a downward direction at the downstream side of gravel crests, while net upward turbulent momentum flux generally occurs upstream of gravel particle crests. These spatial variations correspond to the presence of sweep and ejection events in the zones downstream and upstream of the gravel crests, respectively.
2. Analysis of the extended Wei & Willmarth's [28] method shows that above gravel crests and far from the bed, net vertical turbulent momentum flux is generally upward, while below gravel crests net turbulent momentum flux is mostly in the downward direction. It was also found that net vertical form-induced momentum flux is significant only near and below gravel crests ($z/H < 0.1$) and occurs in an upward direction toward the water column. This net upward form-induced momentum flux is approximately the same order of magnitude as the turbulent net momentum flux. So,

in the upper part of the roughness layer (approximating the form-induced sub-layer) there is upward total net vertical momentum flux due to the positive turbulent and form-induced vertical momentum fluxes. While, in the lower part of the roughness layer (approximating the interfacial sub-layer), despite positive form-induced net vertical momentum flux, negative turbulent vertical momentum flux leads to the negative total net vertical momentum flux.

3. Comparison between the results of quadrant analysis and the extended Wei & Willmarth [28]'s method shows that net upward turbulent vertical momentum flux between the free surface and $z/H > 0.45$, which results from competition between very weak sweep and ejection events, can maintain particles in suspension mode. In contrast, in the lower part of the roughness layer ($z/H < -0.1$) net downward turbulent vertical momentum flux, resulting from intense sweep and ejection events, can bring pulse of fast flowing water with low sediment concentration down to the bed.
4. Finally, there is also an intermediate layer around gravel crests ($-0.1 < z/H < 0.1$) where intense sweep and ejection events prevail. In the lower part of this layer $-0.1 < z/H < 0.0$, it is found that while the contribution of sweep events to Reynolds shear stress is higher than ejection events, the contribution of sweep events to vertical momentum flux is lower than ejection events. In contrast, above gravel crests, the contribution of ejection events to both Reynolds shear stress and vertical turbulent momentum flux is higher than from sweep events. This means that below gravel crests, ejection events can lift up fine particles, but they can not cause significant longitudinal transport of fine particles until those fine particles reach the gravel crests.

## Acknowledgements

This work has been partially carried out within the SMART Joint Doctorate (Science for the MAnagement of Rivers and their Tidal systems) funded with the support of the Erasmus Mundus program of the European Union. The experiments were funded by the PAT (Autonomy Provence of Trento-Italy) for University Research-2010. The authors are grateful to Dr. Silvano Grizzi and Professor Vladimir Nikora for precious discussions and support in PIV data processing and analysis. We also thank the reviewers, especially Professor Francesco Ballio for their useful comments.

## References

[1] U. Schälchi, The clogging of coarse gravel river beds by fine sediment, Hydrobiologia 235 (1992) 189–197.

[2] E. Wohl, A. Chin, Mountain Rivers: Watershed scale processes and channel morphology, Elsevier, 2006.

[3] R. Grabowski, I. Droppo, G. Wharton, Erodibility of cohesive sediment: The importance of sediment properties, Earth-Science Reviews 105 (3-4) (2011) 101–120.

[4] P. Wood, P. Armitage, Biological effects of fine sediment in the lotic environment, Regulated Rivers: Research and Management 21 (2) (1997) 203–17.

[5] C. Heppell, G. Wharton, J. Cotton, J. Bass, S. Roberts, Sediment storage in the shallow hyporheic of lowland vegetated river reaches, Hydrological Processes 23 (2009) 2239–2251.

[6] T. McCloskey, J. Finnemore, Estimating hydraulic conductivities in an alluvial basin from sediment facies models, Ground Water 34 (6) (1996) 1024–1032.

[7] M. Brunke, T. Gonser, The ecological significance of exchange processes between rivers and groundwater, Freshwater Biology 37 (1997) 1–33.

[8] A. Blaschke, K. Steiner, R. Schmalfuss, D. Gutknecht, D. Sengschmitt, Clogging processes in hyporheic interstices of an impounded river , the Danube at Vienna , Austria, Internat. Rev. Hydrobiol. 88 (2003) 397–413.

[9] P. Wood, P. Armitage, Biological effects of fine sediment in the lotic environment, Regulated Rivers: Research and Management 21 (2) (1997) 203–17.

[10] T. Bo, S. Fenoglio, G. Malacarne, M. Pessino, F. Sgariboldi, Effects of clogging on stream macroinvertebrates: An experimental approach, Limnologica-Ecology and Management of Inland Waters 37 (2) (2007) 186–192.

[11] R. Bagnold, An approach to the sediment transport problem from general physics, USGS Professional Paper 422-I (I) (1966) 37.

[12] A. Sutherland, Proposed mechanism for sediment entrainment by turbulent flows, Journal of Geophysical Research 72 (24) (1967) 6183–6194.

[13] Y. Niño, M. Garcia, Experiments on particle wall region of an open channel flow: implications for sediment transport, Journal of Fluid Mechanics 326 (1996) 285–319.

[14] A. Papanicolaou, P. Diplas, C. Dancey, M. Balakrishnan, Surface roughness effects in near-bed turbulence: Implications to sediment entrainment, Journal of Engineering Mechanics 127 (3) (2001) 211–218.

[15] S. Kline, W. Reynolds, F. Schraub, P. Runstadler, The structure of turbulent boundary layers, Journal of Fluid Mechanics 30 (1967) 741–773.

[16] J. Nelson, R. Shreve, S. McLean, T. Drake, Role of near-bed turbulence structure in bed load transport and bed form mechanics, Water Resources Research 31 (8) (1995) 2071–2086.

[17] H. Nakagawa, I. Nezu, Turbulence in Open Channel Flows, IAHR Monographs, Taylor & Francis, 1993.

[18] A. Thomas, M. Bull, On the role of wall-pressure fluctuations in deterministic motions in the turbulent boundary layer, Journal of Fluid Mechanics 128 (1983) 283–322.

[19] S. Snarski, R. Lueptow, Wall pressure and coherent structures in a turbulent boundary layer on a cylinder in axial flow, Journal of Fluid Mechanics 286 (1995) 137–171.

[20] A. Dwivedi, B. Melville, A. Shamseldin, Hydrodynamic forces generated on a spherical sediment particle during entrainment, Journal of Hydraulic Engineering 136 (10) (2010) 756 – 769.

[21] M. Detert, V. Nikora, G. Jirka, Synoptic velocity and pressure fields at the water-sediment interface of streambeds, Journal of Fluid Mechanics 660 (2010) 55–86.

[22] A. Dwivedi, B. Melville, A. Shamseldin, T. Guha, Flow structures and hydrodynamic force during sediment entrainment, Water resources research 47 (2011) W01509.

[23] A. Radice, V. Nikora, J. Campagnol, F. Ballio, Active interactions between turbulence and bed load: Conceptual picture and experimental evidence, Water Resources Research 49 (1) (2013) 90–99.

[24] R. Adrian, C. Meinhart, C. Tomkins, Vortex organization in the outer region of the turbulent boundary layer, Journal of Fluid Mechanics 422 (2000) 1–54.

[25] A. Shvidchenko, G. Pender, Macroturbulent structure of open-channel flow over gravel beds, Water Resources Research 37 (3) (2001) 709–719.

[26] A. Tamburrino, J. Gulliver, Free-surface visualization of streamwise vortices in a channel flow, Water Resources Research 43 (11) (2007) n/a–n/a.

[27] A. Grass, Structural features of turbulent flow over smooth and rough boundaries, Journal of Fluid Mechanics 50 (1971) 233–255.

[28] T. Wei, W. Willmarth, Examination of v-velocity fluctuations in a turbulent channel flow in the context of sediment transport, Journal of Fluid Mechanics 223 (1991) 241–252.

[29] S. Bennett, J. Bridge, J. Best, Fluid and sediment dynamics of upper stage plane beds, Journal of Geophysical Research: Oceans 103 (C1) (1998) 1239–1274.

[30] M. Righetti, G. Romano, Particle-fluid interactions in a plane near-wall turbulent flow, Journal of Fluid Mechanics 505 (2004) 93–121.

[31] K. Singh, N. Sandham, J. Williams, Numerical simulation of flow over a rough bed, Journal of Hydraulic Engineering 133 (4) (2007) 386–398.

[32] T. Drake, R. Shreve, W. Dietrich, P. Whiting, L. Leopold, Bedload transport of fine gravel observed by motion-picture photography, Journal of Fluid Mechanics 192 (1988) 193–217.

[33] G. Sterk, A. Jacobs, J. Van Boxel, The effect of turbulent flow structures on saltation sand transport in the atmospheric boundary layer, Earth Surface Processes and Landforms 23 (10) (1998) 877–887.

[34] P. Bandyopadhyay, R. Watson, Structure of rough-wall turbulent boundary layers, Physics of Fluids (1958-1988) 31 (7) (1988) 1877–1883.

[35] S. Bomminayuni, T. Stoesser, Turbulence statistics in an open-channel flow over a rough bed, Journal of Hydraulic Engineering 137 (11) (2011) 1347–1358.

[36] M. Guala, C. Tomkins, K. Christensen, R. Adrian, Vortex organization in a turbulent boundary layer overlying sparse roughness elements, Journal of Hydraulic Research 50 (5) (2012) 465–481.

[37] R. S. Raupach M., Antonia R., Rough-wall turbulent boundary layers, Applied Mechanics Review 44 (1991) 1–25.

[38] J. Jimenez, Turbulent flows over rough walls, Annual Review of Fluid Mechanics 36 (1) (2004) 173–196.

[39] V. Nikora, D. Goring, I. McEwan, G. Griffiths, Spatially averaged open-channel flow over rough bed, Journal of Hydraulic Engineering 127 (2) (2001) 123–133.

[40] T. Buffin-Bélanger, S. Rice, I. Reid, J. Lancaster, Spatial heterogeneity of near-bed hydraulics above a patch of river gravel, Water Resources Research 42 (4) (2006) n/a–n/a.

[41] S. McLean, V. Nikora, Characteristics of turbulent unidirectional flow over rough beds: Double-averaging perspective with particular focus on sand dunes and gravel beds, Water Resources Research 42 (10) (2006) n/a–n/a.

[42] J. Finnigan, Turbulence in plant canopies, Annual Review of Fluid Mechanics 32 (1) (2000) 519–571.

[43] M. Righetti, A. Armanini, Flow resistance in open channel flows with sparsely distributed bushes, Journal of Hydrology 269 (1-2) (2002) 55–64.

[44] V. Nikora, I. McEwan, S. McLean, S. Coleman, D. Pokrajac, R. Walters, Double-averaging concept for rough-bed open-channel and overland flows: Theoretical background, Journal of Hydraulic Engineering 133 (8) (2007) 873–883.

[45] D. Pokrajac, L. Campbell, V. Nikora, C. Manes, I. McEwan, Quadrant analysis of persistent spatial velocity perturbations over square-bar roughness, Experiments in Fluids 42 (3) (2007) 413–423.

[46] I. Nezu, M. Sanjou, PIV and PTV measurements in hydro-sciences with focus on turbulent open-channel flows, Journal of Hydro-environment Research 5 (4) (2011) 215 – 230.

[47] V. Weitbrecht, D. Seol, E. Negretti, M. Detert, G. Kühn, G. Jirka, PIV measurements in environmental flows: Recent experiences at the institute

for hydromechanics in karlsruhe, Journal of Hydro-environment Research 5 (4) (2011) 231 – 245.

[48] M. Leeder, On the dynamics of sediment suspension by residual Reynolds stresses-confirmation of bagnold's theory, Sedimentology 30 (4) (1983) 485–491.

[49] T. Wei, W. Willmarth, Reynolds-number effects on the structure of a turbulent channel flow, Journal of Fluid Mechanics 204 (1989) 57–95.

[50] K. Christensen, R. Adrian, Statistical evidence of hairpin vortex packets in wall turbulence, Journal of Fluid Mechanics 431 (2001) 433–443.

[51] E. Mignot, D. Hurther, E. Barthelemy, On the structure of shear stress and turbulent kinetic energy flux across the roughness layer of a gravel-bed channel flow, Journal of Fluid Mechanics 638 (2009) 423–452.

[52] S. Lu, W. Willmarth, Measurements of the structure of the reynolds stress in a turbulent boundary layer, Journal of Fluid Mechanics 60 (1973) 481–511.

[53] R. Narasimha, R. Kumar, A. Prabhu, S. Kailas, Turbulent flux events in a nearly neutral atmospheric boundary layer, Philosophical Transactions of the Royal Society A: Mathematical, Physical and Engineering Sciences 365 (1852) (2007) 841–858.

[54] W. Willmarth, S. Lu, Structure of the reynolds stress near the wall, Journal of Fluid Mechanics 55 (1972) 65–92.

[55] D. Bogard, W. Tiederman, Burst detection with single-point velocity measurements, Journal of Fluid Mechanics 162 (1986) 389–413.

[56] R. Hardy, J. Best, S. Lane, P. Carbonneau, Coherent flow structures in a depth-limited flow over a gravel surface: The role of near-bed turbulence and influence of reynolds number, Journal of Geophysical Research: Earth Surface 114 (F1) (2009) n/a–n/a.

[57] V. Nikora, D. Goring, B. Biggs, On gravel-bed roughness characterization, Water Resources Research 34 (3) (1998) 517–527.

[58] J. Aberle, Measurements of armour layer roughness geometry function and porosity, Acta Geophysica 55 (1) (2007) 23–32.

[59] S. H. Mohajeri, S. Grizzi, M. Righetti, G. P. Romano, V. Nikora, The structure of gravel-bed flow with intermediate submergence: A laboratory study, Water Resources Research 51 (11) (2015) 9232–9255.

[60] Wiberg, S. J., Velocity distribution and bed roughness in high gradient streams, Water Resources Research 27 (1994) 825 – 838.

[61] H. Schlichting, K. Gersten, Boundary-Layer Theory, Springer, 2000.

[62] V. Nikora, I. McEwan, S. McLean, S. Coleman, D. Pokrajac, R. Walters, Double-averaging concept for rough-bed open-channel and overland flows: Theoretical background, Journal of Hydraulic Engineering 133 (8) (2007) 873–883.

[63] C. Manes, D. Pokrajac, I. McEwan, Double-averaged open-channel flows with small relative submergence, Journal of Hydraulic Engineering 133 (8) (2007) 896–904.

[64] V. Nikora, D. Goring, B. Biggs, Silverstream eco-hydraulics flume: Hydraulic design and tests, New Zealand Journal of Marine and Freshwater Research 32 (4) (1998) 607–620.

[65] J. Cooper, S. Tait, Spatially representative velocity measurement over water-worked gravel beds, Water Resources Research 46 (11) (2010) n/a–n/a.

[66] L. Benedict, R. Gould, Towards better uncertainty estimates for turbulence statistics, Experiments in Fluids 22 (2) (1996) 129–136.

[67] D. DiFlorio, F. DiFelice, G. Romano, Windowing, re-shaping and re-orientation interrogation windows in particle image velocimetry for the

investigation of shear flows, Measurement Science and Technology 13 (7) (2002) 953.

[68] F. Scarano, Iterative image deformation methods in piv, Measurement Science and Technology 13 (1) (2002) R1.

[69] J. Westerweel, F. Scarano, Universal outlier detection for piv data, Experiments in Fluids 39 (6) (2005) 1096–1100.

[70] S. Soloff, R. Adrian, Z. Liu, Distortion compensation for generalized stereoscopic particle image velocimetry, Measurement Science and Technology 8 (12) (1997) 1441.

[71] A. Prasad, R. Adrian, C. Landreth, P. Offutt, Effect of resolution on the speed and accuracy of particle image velocimetry interrogation, Experiments in Fluids 13 (2-3) (1992) 105–116.

[72] S. H. Mohajeri, Hydrodynamics of gravel bed flows (implication on colmation), Ph.D. thesis, University of Trento and Queen Mary University of London (2014).

[73] S. Dey, R. Das, Gravel-bed hydrodynamics: Double-averaging approach, Journal of Hydraulic Engineering 138 (8) (2012) 707–725.

[74] C. Dancey, M. Balakrishnan, P. Diplas, T. Papanicolaou, The spatial inhomogeneity of turbulence above a fully rough, packed bed in open channel flow, Experiments in Fluids 29 (4) (2000) 402–410.

[75] S. Sarkar, S. Dey, Double-averaging turbulence characteristics in flows over a gravel bed, Journal of Hydraulic Research 48 (6) (2010) 801–809.

[76] R. Hardy, S. Lane, R. Ferguson, D. Parsons, Emergence of coherent flow structures over a gravel surface: A numerical experiment, Water Resources Research 43 (3) (2007) n/a–n/a.

[77] M. Leeder, T. Gray, J. Alexander, Sediment suspension dynamics and a new criterion for the maintenance of turbulent suspensions, Sedimentology 52 (4) (2005) 683–691. `doi:10.1111/j.1365-3091.2005.00720.x`.

[78] J. Jeong, F. Hussain, W. Schoppa, J. Kim, Coherent structures near the wall in a turbulent channel flow, Journal of Fluid Mechanics 332 (1997) 185–214.

[79] R. Adrian, K. Christensen, Z. Liu, Analysis and interpretation of instantaneous turbulent velocity fields, Experiments in Fluids 29 (3) (2000) 275–290. `doi:10.1007/s003489900087`.

[80] J. Cooper, S. Tait, The spatial organisation of time-averaged streamwise velocity and its correlation with the surface topography of water-worked gravel beds, Acta Geophysica 56 (3) (2008) 614–641.

[81] W. Graf, Hydraulics of sediment transport, McGraw-Hill series in water resources and environmental engineering, McGraw-Hill, 1971.